Eur. Phys. J. Plus (2023) 138:121
https://doi.org/10.1140/epjp/s13360-023-03742-7

THE EUROPEAN PHYSICAL JOURNAL PLUS

Regular Article

Optical properties of $Al_xIn_yGa_{1-x-y}As/Al_zGa_wIn_{1-z-w}As$ quantum wells under electric and magnetic fields for telecommunication applications

E. Kaynar[1], **B. O. Alaydin**[1,2,a]

[1] Nanophotonic Application and Research Center, Sivas Cumhuriyet University, 58140 Sivas, Türkiye
[2] Department of Electronics and Automation, Sivas Vocational College, Sivas Cumhuriyet University, 58140 Sivas, Türkiye

Received: 6 October 2022 / Accepted: 24 January 2023
© The Author(s), under exclusive licence to Società Italiana di Fisica and Springer-Verlag GmbH Germany, part of Springer Nature 2023

Abstract In this paper, we have designed $Al_xIn_yGa_{1-x-y}As/Al_zGa_wIn_{1-z-w}As$ quantum well structure having absorption at the telecom band of 1.55 µm. Interband absorption coefficients have been calculated under applied electric and magnetic fields. First, electronic band structure and corresponding energy states for electrons, heavy holes and light holes in the conduction and valance bands have been obtained by solving the one-dimensional time-independent Schrödinger equation. The effects of the electric and magnetic fields on the electron energy levels have been investigated using the finite element method under the effective mass approximation. The magnetic field, which bends band edges, has no major effect on the localization of the electronic states. On the other hand, the electric field causes the localization of all electronic states in different quantum wells. It has been observed that many interband transitions are possible without applied electric and magnetic fields. Absorption occurs from heavy (light) holes to electron states. This causes uncontrolled (undirected) absorption of photon energy between the energy levels. When the electric field is applied, it significantly affects the absorption coefficient and the absorption coefficient values of e_1-hh_2, e_2-hh_1, e_2-hh_3, e_2-lh_1, e_2-lh_3, e_3-hh_2 and e_3-lh_2 cross out due to very sharp decrease in the dipole moment matrix elements but e_1-hh_1, e_1-lh_1 and e_3-lh_3 transitions have emerged and become very strong at 20 kV/cm electric field intensity. The magnetic field causes a negligible small decrease in the optical absorption coefficient. The e_1-hh_2 transition vanishes due to zero dipole moment matrix elements. As compared to the electric field, the magnetic field is not usable for single-wavelength absorption.

1 Introduction

Since the invention of light-emitting semiconductor devices, lasers and light-emitting diodes (LED) have been studied extensively. However, obtaining these devices at desired qualities requires a very broad knowledge of theoretical design, epitaxial crystal growth process and fabrication. Computational tools have enabled theoretical designs. At the same time, superior performances of the epitaxial crystal growth techniques, such as molecular beam epitaxy and metalorganic chemical vapor deposition, have made it possible to obtain very low defect density crystals. In addition, the development of fabrication tools for metallization, etching and photolithography systems has opened a way to build very precise submicron nanoscale devices that low-dimensional devices have been produced.

In the literature, the state-of-the-art performances have been shown for wavelengths from deep ultraviolet (DUV) to the THz region. Tian et al. [1] investigated the interaction and interband transition between various active sites for AlGaN-based deep-ultraviolet LED. They reported that transverse electric polarized DUV light can be obtained using very thin quantum wells (QWs), and the emission wavelength can be tuned down further by increasing the AlN composition in very thin quantum barriers for DUV LEDs. Ghods et al. [2] has shown enhancement in electrical and optical properties of the GaN blue light-emitting diodes. They have used density functional theory to describe the effect of native point defects in their study. Piprek et al. [3] published a study about GaN-based bipolar cascade lasers; they focused on self-consistent numerical simulation and optimization parameters. Symmetric and asymmetric broad-area laser designs both theoretically and experimentally were investigated for the power loss paths for 808 nm single-emitter lasers by Lan et al. [4]. Alaydin et al. [5] studied interband transitions dependent on indium concentration in $Ga_{1-x}In_xAs/GaAs$ asymmetric triple quantum wells. Parasitic flux suppression was theoretically analyzed by Zubov et al. [6] for GaAs-based laser diode emitting at 980 nm. While emission mechanism of the single mode vertical external-cavity surface-emitting lasers around 1030 nm was deeply analyzed by Waldburger et al. [7], Mangold et al. [8] showed design guidelines of the mode-locked integrated external-cavity surface-emitting lasers. Theoretical calculations regarding the cavity length and reflectivity of the facets were performed and verified using a measurement series by Hoppe et al. [9] for GaSb-based digital distributed feedback filter laser diodes. Yang et al. [10] investigated InAs-Based Interband Cascade Lasers (ICLs), where InAs-based ICLs with low threshold current

[a] e-mail: balaydin@cumhuriyet.edu.tr (corresponding author)

Published online: 04 February 2023

density were demonstrated for the first time at wavelengths longer than 6 μm. Moreover, ICLs have continuous-wave (cw) operation at room temperature. Mid-Infrared quantum cascade laser frequency combs have been both experimentally and theoretically studied by Kapsalidis et al. [11]. In the end, THz quantum cascade laser frequency combs based on planarized waveguides were investigated by Senica et al. [12]. According to the studies in the literature, the electromagnetic spectrum for light-emitting and absorbing devices has comprehensively considered.

As mentioned above in the literature studies, there are not much theoretical research for semiconductors operating at telecom wavelengths (around 1.55 μm). In this work, we numerically solved the Schrödinger equation for the $Al_xIn_yGa_{1-x-y}As/Al_zGa_wIn_{1-z-w}As$ triple quantum well (TQW) for 1.55 μm without applying an external fields. Then, we applied both the electric and magnetic fields separately to the quantum wells. Finally, we have investigated the effect of the external fields on the absorption coefficient changes. The numerical simulations for 1.55 μm with or without the applied external fields reveal the novelty of our paper. The paper is organized as follows: in Sect. 1, we have described the method and parameters used in the calculations. In Sect. 2, results and discussions are given. We then finish the paper with a conclusion.

2 Theory

The energy states and corresponding wavefunctions for electrons (ES), heavy holes (HHS) and light holes (LHS) in $Al_xIn_yGa_{1-x-y}As/Al_zGa_wIn_{1-z-w}As$ TQW are obtained by solving the Schrödinger equation under the effective mass approach. $Al_xIn_yGa_{1-x-y}As$ and $Al_zGa_wIn_{1-z-w}As$ quantum barrier and well materials are chosen as lattice match to InP to exclude strain effect on the heavy and light holes otherwise heavy and light hole energy states are shifting up and down dependent on the strain type [13, 14]. The time-independent Hamiltonian of the quantum well region under the electric and magnetic fields is given in Eq. (1) as described in [15–17].

$$H = -\frac{\hbar^2}{2m^*}\frac{d^2}{dz^2} + \frac{e^2B^2z^2}{2m^*c^2}V(z) + ezF_z \tag{1}$$

where $\hbar$ is the reduced Plank constant, m^* is the effective mass of the electron, $V(z)$ is the potential, e is the elemental charge, F indicates the electric field applied parallel to the growth direction (z direction) of the electron and B is the magnetic field intensity applied perpendicular to the growth direction. After deriving the energy states and corresponding wave functions, the linear and third-order interband absorption coefficients, obtained from the compact density matrix formalism, are calculated as follows [18]:

$$\beta^{(1)}(w) = w\sqrt{\frac{\mu}{\varepsilon_r}}\frac{e^2|M_{ij}|^2\sigma_v\hbar\Gamma_{ij}}{(\Delta E_{ij}-\hbar w)^2+(\hbar\Gamma_{ij})^2} \tag{2}$$

$$\beta^{(3)}(w,I) = -2w\sqrt{\frac{\mu}{\varepsilon_r}}\left(\frac{I}{\varepsilon_0 n_\Gamma c}\right)\frac{e^4|M_{ij}|^4\sigma_v\hbar\Gamma_{ij}}{\left((\Delta E_{ij}-\hbar w)^2+(\hbar\Gamma_1 j)^2\right)^2}\left(1-\frac{|M_{jj}-M_{ii}|}{|2M_{ii}|^2}\frac{(\Delta E_{ij}-\hbar w)^2-(\hbar\Gamma_{ij})^2+2\Delta E_{ij}(\Delta E_{ij}-\hbar w)}{\Delta E_{ij}^2+\hbar\Gamma_{ij}^2}\right) \tag{3}$$

where w represents the angular frequency and Γ_{ij} is the relaxation time for interband transitions, μ represents the magnetic permeability, ε_r is the real part of the electrical permittivity and σ_v is the electron density. The transition energy between the excited and ground energy state of the electron is defined as ΔE_{ij}. M_{ij} represents the transition dipole element and is given as [19]:

$$M_{ij} = \left|\left\langle\psi_f^*(z)|z|\psi_i(z)\right\rangle\right| \tag{4}$$

3 Results and discussion

The parameters used in our calculations are as follows: 0.07927 m_0 is the electron effective mass for InP (m_0 is free electron mass), 0.409 m_0 is the heavy hole effective mass for InP, 0.0902 m_0 is the light hole effective mass for InP, $L_w = 100$ Å is the width of the quantum well, $L_b = 20$ Å is the barrier width and potential heights are $V_c = 510$meV and $V_v = 201$meV. Potential height is calculated by using the Vegard's law, and parameters are taken from reference [20]. Refractive index, susceptibility, the transition time of carriers and frequency are taken as $n_r = 3.2510$, $\mu = 4\pi \times 10^{-7}\text{Hm}^{-1}$, $T_{12} = 0.14$ps, $\Gamma_{12} = \frac{1}{T_{12}}$. In TQW heterojunction, the electron states (ES) are split into three energy states (quasi-triple) as shown in Fig. 1. The potential heights are the same since the indium concentrations are equal. The first three bounded conduction band energy states in the absence of applied electric field and for varying electric field intensities as $F = 20$kV/cm and $F = 40$kV/cm, respectively.

The distribution of probability density of wavefunctions (PDW) within the wells is separated. Ground state PDW is mostly found in the second quantum well (QW) but it is also distributed in the first and third QW. When an electric field is applied to the quantum

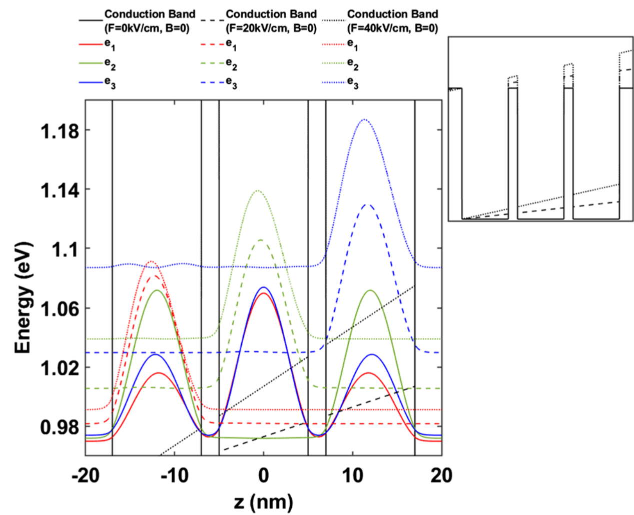

Fig. 1 Energy states for conduction band and $F = 0\text{kV/cm}$, $F = 20\text{kV/cm}$ and $F = 40\text{kV/cm}$, respectively

Table 1 Energy states for $F = 0\text{kV/cm}$, $F = 20\text{kV/cm}$ and $F = 40\text{kV/cm}$, respectively

E(eV) ($F = 0$ kV/cm, $B = 0$ T)	$e_1 = 0.031$	$e_2 = 0.033$	$e_3 = 0.035$
E(eV) ($F = 20$ kV/cm, $B = 0$ T)	$e_1 = 0.043$	$e_2 = 0.067$	$e_3 = 0.091$
E(eV) ($F = 40$ kV/cm, $B = 0$ T)	$e_1 = 0.052$	$e_2 = 0.100$	$e_3 = 0.148$

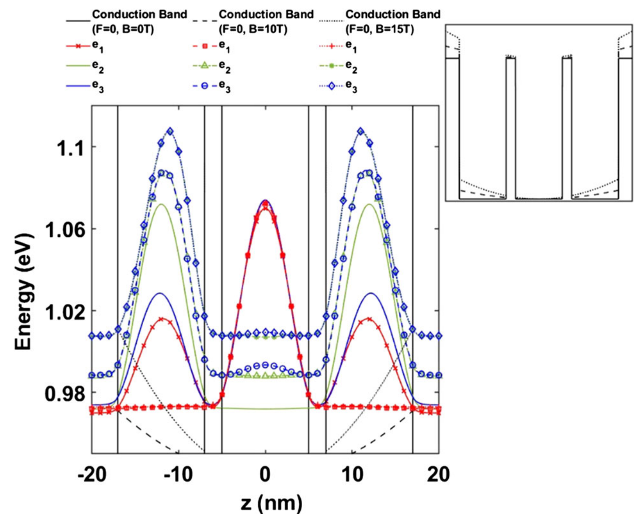

Fig. 2 First three bounded energy states for conduction band under applied magnetic fields for $B = 0\text{T}$, $B = 10\text{T}$ and $B = 15\text{T}$, respectively

wells, the wells are tilted proportional to electric field intensity (EFI). The ES of the e_1 state moves to the first QW to reach minimum energy, and the energy eigenvalue shifts up for $F = 20\text{kV/cm}$. As the EFI increases more, there are no changes in the localization of e_1, only the energy eigenvalue shifts up a little bit for $F = 40\text{kV/cm}$. The second excited state behaves almost the same as the ground state. However, the first excited state e_2 has localized in the first and third QW even for narrow quantum barrier (QB) height in case of zero EFI. This indicates only possible interband transition from e_2 can happen from the first and third QWs. When the electric field is applied ($F = 20\text{kV/cm}$), localization of the e_2 solely happens in the second QW, which only allows interband transition through the second QW. Further increase in EFI ($F = 40\text{kV/cm}$) results in a higher e_2 eigenvalue, localization is not affected by EFI. e_3 localizes the same as the e_1 without applied EFI but when EFI 20 kV/cm is applied, e_3 localizes in the third QW, and energy eigenvalue shifts up to higher than other energy states due to higher kinetic energy. Higher EFI does not affect the localization of the e_3 but enhances energy eigenvalue. In the end, the electric field causes localization of each energy state in different QWs; this indicates zero overlap and intraband transition in between subbands which promote the possibility of the interband transition. In Table 1, energy eigenvalues are given for $F = 0\text{kV/cm}$, $F = 20\text{kV/cm}$ and $F = 40\text{kV/cm}$ for ES, respectively.

Figure 2 shows the first three bounded conduction band energy states in the absence of an applied magnetic field and for $B = 10\text{T}$ and $B = 15\text{T}$, respectively. When the magnetic field is applied, the barriers are bent proportionally with magnetic field intensity (MFI). At first, localization of the e_1 state distributes in all QWs; then, it moves to the second QW for $B = 10$ T. When the MFI increases further, the localization of e_1 does not change. The energy eigenvalues for $B = 10$ T and $B = 15$ T are the same as shown in Table 2. When the magnetic field is applied ($B = 10$ T), the localization of e_2 occurs at the first and third QWs. The energy

Table 2 Energy states for $B = 10$T and $B = 15$T, respectively

E(eV) ($F = 0$ kV/cm, $B = 10$ T)	$e_1 = 0.033$	$e_2 = 0.049$	$e_3 = 0.049$
E(eV) ($F = 0$ kV/cm, $B = 15$ T)	$e_1 = 0.034$	$e_2 = 0.068$	$e_3 = 0.069$

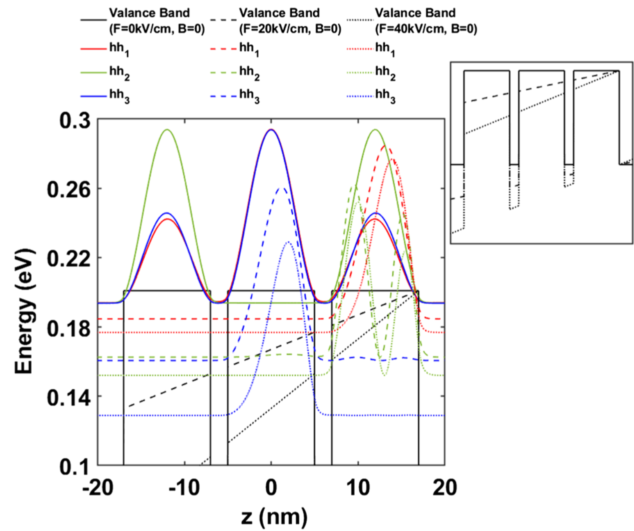

Fig. 3 Energy states for valance band and heavy hole states for $F = 0$kV/cm, $F = 20$kV/cm and $F = 40$kV/cm, respectively

Table 3 Energy states for HHS $F = 0$kV/cm, $F = 20$kV/cm and $F = 40$kV/cm, respectively

E(eV) ($F = 0$ kV/cm, $B = 0$ T)	$hh_1 = 0.007$	$hh_2 = 0.007$	$hh_3 = 0.007$
E(eV) ($F = 20$ kV/cm, $B = 0$ T)	$hh_1 = 0.016$	$hh_2 = 0.038$	$hh_3 = 0.040$
E(eV) ($F = 40$ kV/cm, $B = 0$ T)	$hh_1 = 0.024$	$hh_2 = 0.049$	$hh_3 = 0.072$

eigenvalue and distribution of the e_2 state are completely matching with the e_3 state as shown in Fig. 2 because of that it is not observable in Fig. 2. The eigenvalues are as given in Table 2. The degeneracy that occurs between e_2 and e_3 states is due to the high quantum barrier and effective mass. Further increase in MFI ($B = 15$ T) results in a higher e_2 eigenvalue (Table 2) but it does not affect the localization so that it matches as in the case of 10 T. e_3 localizes the same as e_1 without applying MFI, but when MFI 10 T is applied e_3 localizes in the first and third QWs. The energy eigenvalue shifts higher than other energy states due to the higher kinetic energy. Higher MFI does not affect the localization of e_3 but increases the energy eigenvalue. In Table 2, energy eigenvalues are given for $B = 10$T and $B = 15$T, respectively.

Figure 3 shows the valance band and corresponding energy states for heavy hole states (HHS) for varying electric field intensities, $F = 0$kV/cm, $F = 20$kV/cm and, $F = 40$kV/cm, respectively. The ground state PDW is mostly located in the second QW, but it is also distributed in the first and third QWs. When an electric field is applied to quantum wells, the wells are tilted proportionally to the EFI. The localization of the hh_1 state moves to the third QW, and the energy eigenvalue shifts down for $F = 20$ kV/cm. As the EFI increases further, the localization of hh_1 shifts slightly to the right, and the energy eigenvalue for $F = 40$ kV/cm shifts slightly down a bit more. The first excited heavy hole (hh_2) state localizes in the first and third QW even for the narrow quantum barrier (QB) height in the zero EFI state. This indicates that only possible cross-band transition from hh_2 can occur from the first and third QWs. When the electric field is applied ($F = 20$ kV/cm), the localization of hh_2 takes place only in the third QW, allowing interband transition from the last QW only. In addition, branching is observed for hh_2 which results in partial non-localization in the third QW. Further increase in EFI ($F = 40$ kV/cm) results in a lower hh_2 eigenvalue and localization is unaffected by the EFI. hh_3 (second excited heavy hole state) localizes the same as hh_1 without applying EFI, but when applying EFI 20 kV/cm, hh_3 fully localizes in the second QW. Its energy eigenvalue shifts to deeper energy states. Higher EFI has no effect on the localization of hh_3 except for a slight shift to the right in the QW region but increases its energy eigenvalue. In Table 3, energy eigenvalues are given for $F = 0$kV/cm, $F = 20$kV/cm and $F = 40$kV/cm for HHS, respectively. It is seen that there is a strong degeneracy for the energy eigenvalues of the heavy holes originating due to heavy effective mass values.

Figure 4 shows the valance band and energy state for HHS in the absence of a magnetic field and applying the $B = 10$T and $B = 15$T magnetic fields, respectively. When a magnetic field is applied to QW, the wells are bent proportionally with the MFI. The applied magnetic field for $B = 10$ T, the hh_1 state moves to the second QW. As the MFI increases further, there is no change in the localization of hh_1. hh_1 for $B = 10$ T and hh_1 for $B = 15$ T overlap exactly at the same eigenvalue. The first excited (hh_2) localizes in the first and third QW in the zero MFI state. This indicates that only possible cross-band transition from hh_2 can occur to the first and third QWs (beneath the hh_3 in Fig. 4). When the magnetic field is applied ($B = 10$ T), the localization of hh_2 occurs at the first and third QWs, resulting in a lower hh_2 eigenvalue. Further increase in MFI ($B = 15$ T) results in a higher hh_2 eigenvalue, and localization is unaffected by MFI. hh_3 localizes the same as hh_1 without applying MFI. However, hh_3 is localized in the first and

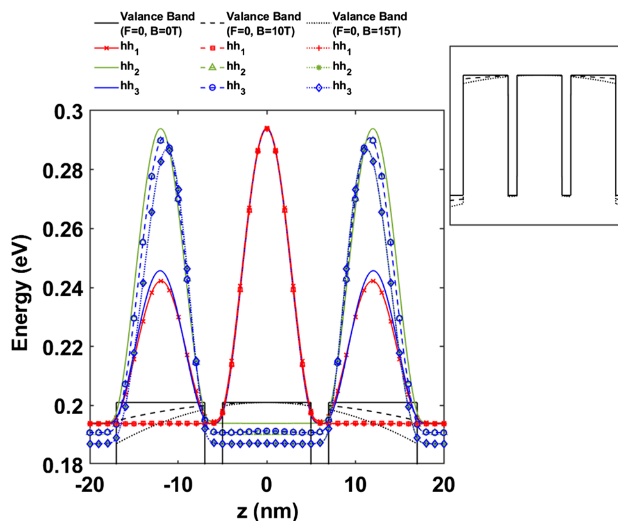

Fig. 4 Valance band energy states for HHS at $B = 0$T, $B = 10$T and $B = 15$T, respectively

Table 4 Energy states for HHS B = 10T and B = 15T, respectively

E(eV) ($F = 0$ kV/cm, $B = 10$ T)	$hh_1 = 0.007$	$hh_2 = 0.010$	$hh_3 = 0.010$
E(eV) ($F = 0$ kV/cm, $B = 15$ T)	$hh_1 = 0.007$	$hh_2 = 0.014$	$hh_3 = 0.014$

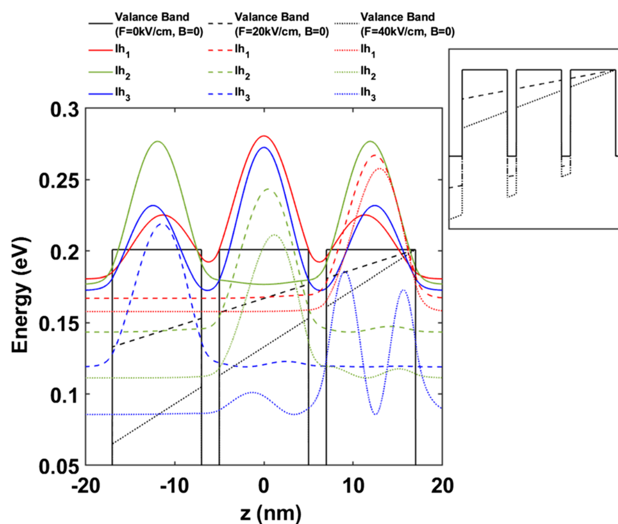

Fig. 5 Valance band energy states light hole states for $F = 0$kV/cm, $F = 20$kV/cm and $F = 40$kV/cm, respectively

third QWs when MFI 10 T is applied. The energy eigenvalue shifts to higher values. Also, for $B = 10$ T, hh_3 and hh_2 localize on top of each other. Higher MFI does not affect the localization of hh_3 but increases its energy eigenvalue. Also, for $B = 15$ T, hh_3 and hh_2 were localized on top of each other. In Table 4, energy eigenvalues are given for $B = 10$T and $B = 10$T HHS, respectively.

Figure 5 shows the valance band energy states for light hole states (LHS) in the absence of an electric field and applying an electric field $F = 20$kV/cm and $F = 40$kV/cm, respectively. The lh_1 state moves to the third QW, and the energy eigenvalue shifts down for $F = 20$ kV/cm. As the EFI increases further, there is no change in the localization of lh_1, only the energy eigenvalue shifts slightly down for $F = 40$ kV/cm. The second excited lh_2 state behaves almost the same as the ground state. However, the first excited state lh_1 localizes in the first and third QW in the case of the zero EFI. When the electric field is applied ($F = 20$ kV/cm), the localization of lh_2 takes place only in the second QW, allowing interband transition only from the second QW. Further increase in EFI ($F = 40$ kV/cm) results in a lower lh_2 eigenvalue; localization is unaffected by EFI. lh_3 localizes in all wells just like lh_1 without applying EFI, but when EFI is applied 20 kV/cm lh_3 completely exists in the first QW, and its energy eigenvalue shifts to deeper. The higher EFI shifts the localization of lh_3 completely to the third QW and decreases the energy eigenvalue. In Table 5, energy eigenvalues are given for $F = 0$kV/cm, $F = 20$kV/cm and $F = 40$kV/cm, respectively.

Figure 6 shows the valance band energy states for the LHS in the absence of a magnetic field and applying the $B = 10$T and $B = 15$T magnetic fields, respectively. The lh_1 state moves to the second QW, and the energy eigenvalue shifts down for $B = 10$ T. As the EFI increases further, there is no change in the localization of lh_1, only the energy eigenvalue shifts slightly down for $B =$ 15 T. The second excited state behaves almost the same as the ground state. However, the first excited state lh_2 is localized in the

Table 5 Energy states for LHS $F = 0\text{kV/cm}$, $F = 20\text{kV/cm}$ and $F = 40\text{kV/cm}$, respectively

E(eV) ($F = 0$ kV/cm, $B = 0$ T)	$lh_1 = 0.0204$	$lh_2 = 0.024$	$lh_3 = 0.028$
E(eV) ($F = 20$ kV/cm, $B = 0$ T)	$lh_1 = 0.034$	$lh_2 = 0.058$	$lh_3 = 0.082$
E(eV) ($F = 40$ kV/cm, $B = 0$ T)	$lh_1 = 0.043$	$lh_2 = 0.090$	$lh_3 = 0.115$

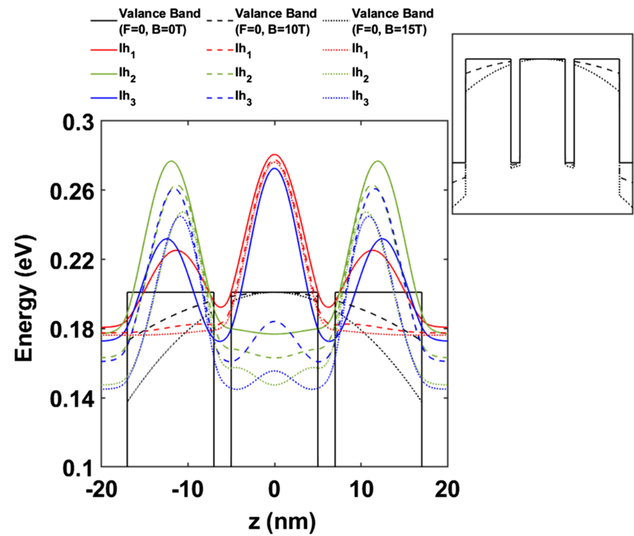

Fig. 6 Energy states for valance band and LHS for $B = 0\text{T}$, $B = 10\text{T}$ and $B = 15\text{T}$, respectively

Table 6 Energy states for LHS $B = 10\text{T}$ and $B = 15\text{T}$, respectively

E(eV) ($F = 0$ kV/cm, $B = 10$ T)	$lh_1 = 0.024$	$lh_2 = 0.038$	$lh_3 = 0.040$
E(eV) ($F = 0$ kV/cm, $B = 15$ T)	$lh_1 = 0.025$	$lh_2 = 0.054$	$lh_3 = 0.056$

first and third QW in the zero EFI state. When the magnetic field ($B = 10$ T) is applied, there is no change in the localization of lh_2, resulting in a higher lh_2 eigenvalue. Further increase in MFI ($B = 15$ T) results in a higher lh_2 eigenvalue and localization is unaffected by MFI. lh_3 localizes in all wells just like lh_1 without applying MFI, but when MFI 10 T is applied lh_3 is again localized in all QWs but less pronounced in the second QW. The higher MFI slightly decreases the localization in the second QW and the energy eigenvalue goes to a deeper value. In Table 6, energy eigenvalues are given for $B = 10\text{T}$ and $B = 15\text{T}$ for LHS, respectively.

M_{ij} represents the dipole moment matrix elements (DMME), Table 7. In semiconductors, interband optical absorption has a shape derived directly from the state density and is proportional to the overlap integral of the conduction and valence bands wavefunctions. As given in Table 7, many transitions have low DMME values, which means that the absorption of photons is not possible in these transitions. Figure 7 shows the absorption coefficients (AC) of the transition from the conduction band ES to the HHS and LHS energy states for zero electric field and for 20 kV/cm, 40 kV/cm but only nonzero absorptions are shown.

The absorption coefficient and energy values of the transition from conduction band ES to HHS and LHS are different from each other. This result is due to the fact that the different effective mass values used in the calculations. Because of this, the HHS and LHS have different localizations in QW, which causes different transitions. Electric field significantly affects the optical absorption spectra in quantum wells and changes optical absorption significantly. When the EFI increases, the AC values of e1−hh2, e2−hh1, e2−hh3, e2–lh1, e2−lh3, e3−hh2 and e3−lh2 transitions drop down to 0 due to very sharp decrease in the DMME. At the same time, AC of the e1−hh1, e1−lh1 and e3−lh3 transitions have emerged and become very strong at 20 kV/cm electric field intensity. As the EFI increases further, the quantum well is tilted more and all energy states are displaced a bit more resulting in the extinction of the e1−lh2 and e3−lh3 transition. ACs of the e1−hh1 and e1−lh1 have become stronger. This result is especially good for a single, powerful and coherent transition, which is very important in laser applications.

Figure 8 shows the ACs of the transition from the conduction band ES to the HHS and LHS when a 10 T and 15 T magnetic field is applied as expected. The bending of quantum barriers increases with increasing MFI resulting in the relocalization of the eigenstates. As can be seen from the figure, the increase in MFI caused a small decrease in the absorption coefficient values. The e_1-hh_2 transition vanishes due to zero DMME, and blueshift occurs. As compared to the electric field, the magnetic field is not usable for single-wavelength absorption.

Table 7 M_{ij} values at different applied electric and magnetic fields

Electric Field Intensity (kV/cm), Magnetic Field Intensity (T) and M_{ij} (nm)				
$F = 0, B = 0$	$F = 20, B = 0$	$F = 40, B = 0$	$F = 0, B = 10$	$F = 0, B = 15$
$e_1-hh_1 = 5.6E-6$	$e_1-hh_1 = 12.3$	$e_1-hh_1 = 12.5$	$e_1-hh_1 = 1.3E-11$	$e_1-hh_1 = 1.4E-11$
$e_1-hh_2 = 8.2$	$e_1-hh_2 = 0.3$	$e_1-hh_2 = 1.06$	$e_1-hh_2 = 1.56$	$e_1-hh_2 = 0.79$
$e_1-hh_3 = 3.8E-13$	$e_1-hh_3 = 0.09$	$e_1-hh_3 = 0.05$	$e_1-hh_3 = 1.6E-9$	$e_1-hh_3 = 3.4E-11$
$e_1-lh_1 = 3.3E-11$	$e_1-lh_1 = 12.05$	$e_1-lh_1 = 12.38$	$e_1-lh_1 = 1.0E-12$	$e_1-lh_1 = 0$
$e_1-lh_2 = 8.31$	$e_1-lh_2 = 1.63$	$e_1-lh_2 = 1.07$	$e_1-lh_2 = 1.85$	$e_1-lh_2 = 1.24$
$e_1-lh_3 = 4.9E-11$	$e_1-lh_3 = 0.29$	$e_1-lh_3 = 1.33$	$e_1-lh_3 = 1.6E-11$	$e_1-lh_3 = 2.5E-11$
$e_2-hh_1 = 8.42$	$e_2-hh_1 = 0.88$	$e_2-hh_1 = 0.68$	$e_2-hh_1 = 0.65$	$e_2-hh_1 = 0.42$
$e_2-hh_2 = 5.1E-11$	$e_2-hh_2 = 0.52$	$e_2-hh_2 = 0.60$	$e_2-hh_2 = 1.3E-8$	$e_2-hh_2 = 1.5E-9$
$e_2-hh_3 = 8.49$	$e_2-hh_3 = 0.42$	$e_2-hh_3 = 0.92$	$e_2-hh_3 = 11.70$	$e_2-hh_3 = 11.41$
$e_2-lh_1 = 8.00$	$e_2-lh_1 = 0.66$	$e_2-lh_1 = 0.42$	$e_2-lh_1 = 3.18$	$e_2-lh_1 = 1.84$
$e_2-lh_2 = 5.5E-11$	$e_2-lh_2 = 0.32$	$e_2-lh_2 = 0.73$	$e_2-lh_2 = 4.3E-10$	$e_2-lh_2 = 4.8E-10$
$e_2-lh_3 = 8.86$	$e_2-lh_3 = 1.01$	$e_2-lh_3 = 1.05$	$e_2-lh_3 = 11.17$	$e_2-lh_3 = 11.06$
$e_3-hh_1 = 1.6E-15$	$e_3-hh_1 = 0.06$	$e_3-hh_1 = 0.80$	$e_3-hh_1 = 2.5E-11$	$e_3-hh_1 = 3.0E-11$
$e_3-hh_2 = 8.69$	$e_3-hh_2 = 0.08$	$e_3-hh_2 = 1.70$	$e_3-hh_2 = 11.64$	$e_3-hh_2 = 11.43$
$e_3-hh_3 = 4.3E-13$	$e_3-hh_3 = 0.06$	$e_3-hh_3 = 0.16$	$e_3-hh_3 = 1.3E-8$	$e_3-hh_3 = 1.3E-9$
$e_3-lh_1 = 3.7E-11$	$e_3-lh_1 = 0$	$e_3-lh_1 = 0.44$	$e_3-lh_1 = 1.3E-10$	$e_3-lh_1 = 1.3E-10$
$e_3-lh_2 = 8.44$	$e_3-lh_2 = 1.28$	$e_3-lh_2 = 1.11$	$e_3-lh_2 = 11.30$	$e_3-lh_2 = 10.81$
$e_3-lh_3 = 4.7E-11$	$e_3-lh_3 = 11.39$	$e_3-lh_3 = 0.98$	$e_3-lh_3 = 5.9E-10$	$e_3-lh_3 = 7.1E-10$

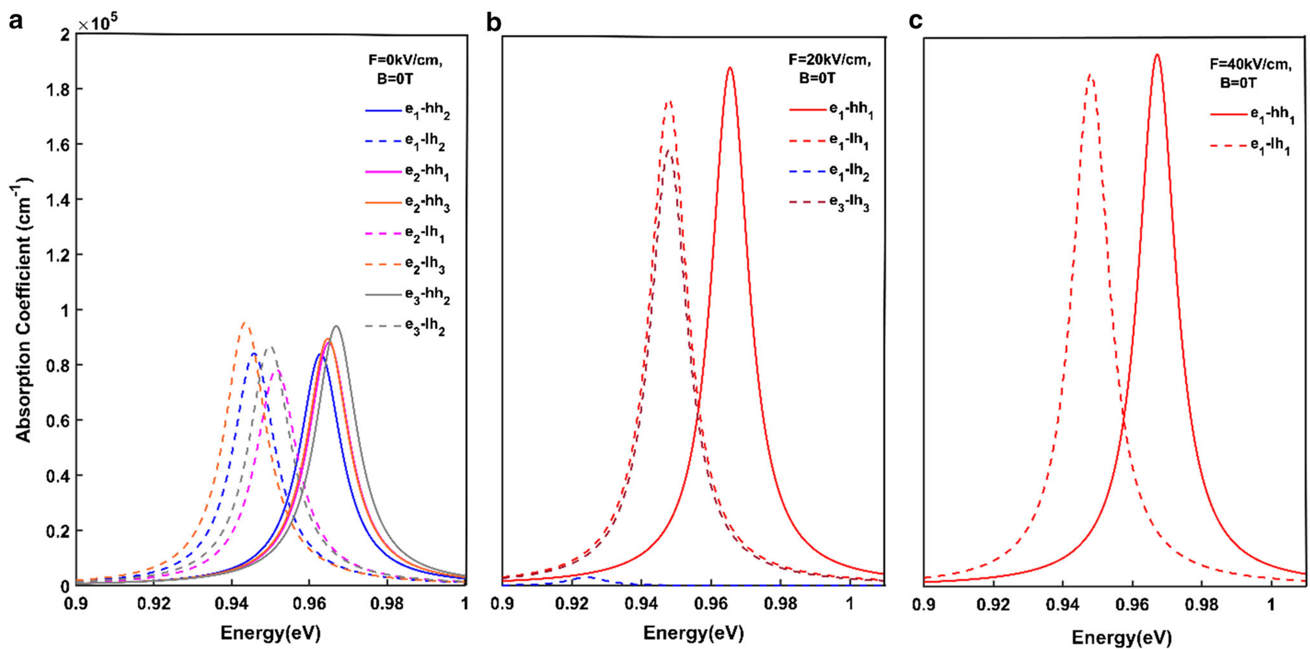

Fig. 7 Absorption coefficients for **a** $F = 0\text{kV/cm},\ B = 0\text{T}$, **b** $F = 20\text{kV/cm},\ B = 0\text{T}$ and **c** $F = 40\text{kV/cm},\ B = 0\text{T}$

4 Conclusion

In conclusion, we have investigated the absorption properties of the $Al_xIn_yGa_{1-x-y}As$ /$Al_zGa_wIn_{1-z-w}As$ quantum well for telecom wavelengths. Energy wavefunctions and corresponding energy eigenvalues have been calculated using the finite element method under effective mass approximation. External fields, electric and magnetic fields, have been applied to study their effect on the transition energy and probability of density wavefunctions. It has been observed that many interband transitions are possible at $F = 0$ and $B = 0$, and absorption happens from heavy (light) holes to electron states. This causes uncontrolled absorption; however, only e_1-hh_1 and e_1-lh_1 are possible when the electric field is applied. This results in single-wavelength absorption which is desired for coherent light emission such as lasers. In addition, EFI increases the absorption coefficient. When the magnetic field is applied, AC

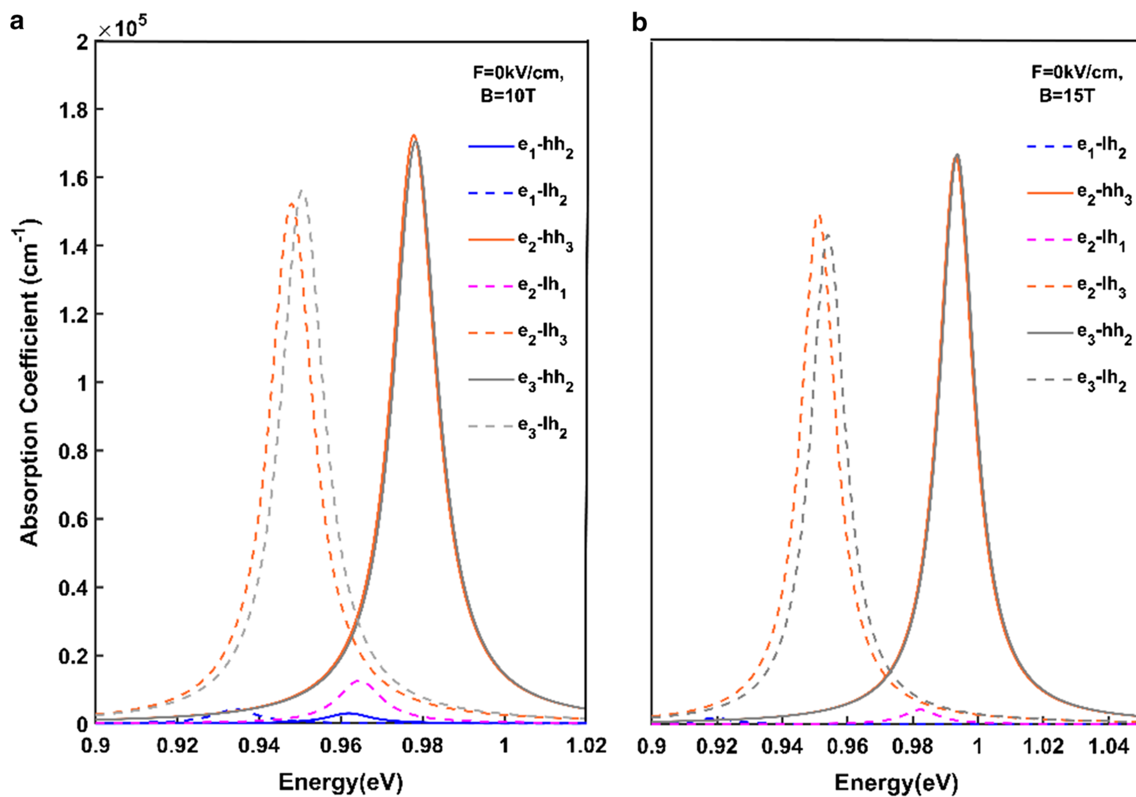

Fig. 8 Absorption coefficients for **a** $F = 0\text{kV/cm}$, $B = 10\text{T}$ and **b** $F = 0\text{kV/cm}$, $B = 15\text{T}$

is almost unchanged and multiple absorption occur which is not desired for device application. Finally, the current study could find usage to design optoelectronic devices by controlling optical properties.

Acknowledgements This study is partly funded by Sivas Cumhuriyet University Scientific Research Project (F-2021-649).

Data Availability Statement The datasets generated during and analyzed during the current study are available from the corresponding author upon reasonable request.

Declarations

Conflict of interest The authors have declared that no conflict of interest exists.

References

1. K. Tian, C. Chu, J. Che, H. Shao, J. Kou, Y. Zhang et al., Interplay between various active regions and the interband transition for AlGaN-based deep-ultraviolet light-emitting diodes to enable a reduced TM-polarized emission. J. Appl. Phys. **126**(24), 245702 (2019). https://doi.org/10.1063/1.5127916
2. A. Ghods, C. Zhou, I.T. Ferguson, Enhancement in electrical and optical properties of field-effect passivated GaN blue light emitting diodes. Semicond. Sci. Technol. **36**(11), 115018 (2021). https://doi.org/10.1088/1361-6641/ac1b12
3. J. Piprek, G. Muziol, M. Siekacz, C. Skierbiszewski, GaN-based bipolar cascade lasers with 25 nm wide quantum wells. Opt. Quant. Electron. **54**(1), 62 (2022). https://doi.org/10.1007/s11082-021-03455-0
4. Y. Lan, G. Yang, Y. Liu, Y. Zhao, Z. Wang, T. Li et al., 808 nm broad-area laser diodes designed for high efficiency at high-temperature operation. Semicond. Sci. Technol. **36**(10), 105012 (2021). https://doi.org/10.1088/1361-6641/ac2160
5. B.O. Alaydin, E. Ozturk, S. Elagoz, Interband transitions dependent on indium concentration in $Ga_{1-x}In_xAs/GaAs$ asymmetric triple quantum wells. Int. J. Mod. Phys. B **32**(05), 1850052 (2018). https://doi.org/10.1142/s0217979218500522
6. F.I. Zubov, M.E. Muretova, A.S. Payusov, M.V. Maximov, A.E. Zhukov, L.V. Asryan, Parasitic recombination in a laser with asymmetric barrier layers. Semiconductors **54**(3), 366–373 (2020). https://doi.org/10.1134/S1063782620030203
7. D. Waldburger, S.M. Link, M. Mangold, C.G.E. Alfieri, E. Gini, M. Golling et al., High-power 100 fs semiconductor disk lasers. Optica. **3**(8), 844–852 (2016). https://doi.org/10.1364/OPTICA.3.000844
8. M. Mangold, V.J. Wittwer, C.A. Zaugg, S.M. Link, M. Golling, B.W. Tilma et al., Femtosecond pulses from a modelocked integrated external-cavity surface emitting laser (MIXSEL). Opt Express. **21**(21), 24904–24911 (2013). https://doi.org/10.1364/OE.21.024904
9. M. Hoppe, C. Aßmann, S. Schmidtmann, T. Milde, M. Honsberg, T. Schanze et al., GaSb-based digital distributed feedback filter laser diodes for gas sensing applications in the mid-infrared region. J. Opt. Soc. Am. B **38**(8), B1–B8 (2021). https://doi.org/10.1364/JOSAB.422517

10. R.Q. Yang, L. Li, W. Huang, S.M.S. Rassel, J.A. Gupta, A. Bezinger et al., InAs-based interband cascade lasers. IEEE J. Sel. Top. Quantum Electron. **25**(6), 1–8 (2019). https://doi.org/10.1109/JSTQE.2019.2916923
11. F. Kapsalidis, B. Schneider, M. Singleton, M. Bertrand, E. Gini, M. Beck et al., Mid-infrared quantum cascade laser frequency combs with a microstrip-like line waveguide geometry. Appl. Phys. **118**(7), 071101 (2021). https://doi.org/10.1063/5.0040882
12. U. Senica, T. Olariu, A. Forrer, P. Micheletti, M. Beck, J. Faist, et al. *THz Quantum Cascade Laser Frequency Combs based on Planarized Waveguides*, in *Conference on Lasers and Electro-Optics* (Optica Publishing Group, San Jose, 2022). p. STu4L.6
13. D. Gershoni, J.M. Vandenberg, R.A. Hamm, H. Temkin, M.B. Panish, Electronic energy levels in InxGa1-xAs/InP strained-layer superlattices. Phys. Rev. B **36**(2), 1320–1323 (1987). https://doi.org/10.1103/PhysRevB.36.1320
14. B. Jogai, P.W. Yu, Energy levels of strained InxGa1-xAs-GaAs superlattices. Phys. Rev. B **41**(18), 12650–12658 (1990). https://doi.org/10.1103/PhysRevB.41.12650
15. D. Altun, O. Ozturk, B.O. Alaydin, E. Ozturk, Linear and nonlinear optical properties of a superlattice with periodically increased well width under electric and magnetic fields. Micro Nanostruct. **166**, 207225 (2022). https://doi.org/10.1016/j.micrna.2022.207225
16. M. Sayrac, Effects of applied external fields on the nonlinear optical rectification, second, and third-harmonic generation in an asymmetrical semi exponential quantum well. Opt. Quant. Electron. **54**(1), 52 (2021). https://doi.org/10.1007/s11082-021-03425-6
17. M. Sayrac, E. Kaynar, F. Ungan, The effect of structure parameters and static electric field on the nonlinear optical properties of triple InGaAs/GaAs quantum well. J. Mol. Struct. **1273**, 134252 (2023). https://doi.org/10.1016/j.molstruc.2022.134252
18. B.O. Alaydin, D. Altun, E. Ozturk, Linear and nonlinear optical properties of semi-elliptical InAs quantum dots: effects of wetting layer thickness and electric field. Thin Solid Films **755**, 139322 (2022). https://doi.org/10.1016/j.tsf.2022.139322
19. B.O. Alaydin, Effect of high bandgap AlAs quantum barrier on electronic and optical properties of $In_{0.70}Ga_{0.30}As/Al_{0.60}In_{0.40}As$ superlattice under applied electric field for laser and detector applications. Int. J. Mod. Phys. B **35**(02), 2150027 (2021). https://doi.org/10.1142/s0217979221500272
20. I. Vurgaftman, J.R. Meyer, L.R. Ram-Mohan, Band parameters for III–V compound semiconductors and their alloys. J. Appl. Phys. **89**(11), 5815–5875 (2001). https://doi.org/10.1063/1.1368156

Springer Nature or its licensor (e.g. a society or other partner) holds exclusive rights to this article under a publishing agreement with the author(s) or other rightsholder(s); author self-archiving of the accepted manuscript version of this article is solely governed by the terms of such publishing agreement and applicable law.